

DRAFT

CMS Internal Note

The content of this note is intended for CMS internal use and distribution only

2009/07/13

Archive Id: 1.7

Archive Date: 2009/07/13 22:16:23

Archive Tag: JP-13-July-2009-a

Alignment of the CMS Muon System with Tracks

Some Cool Dudes² and A. Cern Person¹

¹ CERN

² Some University

Abstract

This paper describes the alignment of the CMS muon chambers using muon tracks from cosmics recorded during CRAFT and from beam halo events recorded during the first circulating beam tests of the LHC.

This box is only visible in draft mode. Please make sure the values below make sense.

PDFAuthor: Some Cool Dudes, A. Cern Person
PDFTitle: Muon Track-based alignment
PDFSubject: CMS
PDFKeywords: CMS, detectors, alignment, tracks

Please also verify that the abstract does not use any user defined symbols

Contents

1	1	Introduction and Geometry	1
2	1.1	Geometry of the muon system	1
3	1.2	Coordinate systems and conventions	3
4	2	DT Internal Alignment	3
5	2.1	Algorithm for General DT Layer Alignment	3
6	2.2	Independent Cross-Check of δ_z	6
7	3	CSC Overlaps Alignment	7
8	3.1	Algorithm	7
9	3.2	Monte Carlo Studies	9
10	3.3	Alignment Results	10
11	4	Global Muon Alignment	10
12	4.1	The HIP Algorithm	10
13	4.2	The MilliPede Algorithm	13
14	4.3	Monte Carlo Study of the Two Algorithms	16
15	4.4	Alignment Results and Cross-Checks	16
16	5	Conclusions	19

1 Introduction and Geometry

The CMS experiment features a large muon tracking system for identifying and reconstructing the momenta of muons. As with all tracking systems, the resolution of reconstructed tracks depends both on the intrinsic resolution of its detector elements and on their alignment. By “alignment,” we mean measurement of the detector elements’ positions and orientations in space, 3 translational plus 3 rotational degrees of freedom, knowledge which allows us to transform hit positions from detector-bound local coordinate systems into global 3-D space.

This paper describes methods for aligning barrel Drift Tube (DT) chambers and endcap Cathode Strip Chambers (CSC) and their internal layers with tracks, as well as results of alignments using cosmic rays and beam-halo tracks from the 2008 LHC run. We will consider two cases: (1) alignment relative to the modular structures from which the muon system is built, and (2) alignment in a single coordinate system defined by the central CMS tracker. Alignment using integrated physical measurement devices such as lasers, calipers, and inclinometers is described elsewhere [1].

1.1 Geometry of the muon system

The muon system is a collection of independent tracking chambers, each of which contains parallel measurement planes called layers. The chambers are mounted on 5 moveable barrel wheels (labeled -2 through $+2$) and 6 endcap disks (3 per endcap). Within these large structures, chambers are arranged in stations, labeled in Figure 1, with azimuthal positions called sectors (in the barrel) or simply chamber number (endcap). Barrel stations 1–3 have 12 sectors, station 4 has 14 sectors, and most rings of chambers in the endcap have 36 chambers, the exceptions being ME2/1, ME3/1, and ME4/1, which have 18.

Barrel DT chambers have two levels of internal structure: superlayers containing 4 layers each. Stations 1–3 have 3 superlayers, the middle one making measurements in a direction orthogonal to the outer two. Station 4 chambers have no middle superlayer (only superlayers 1 and

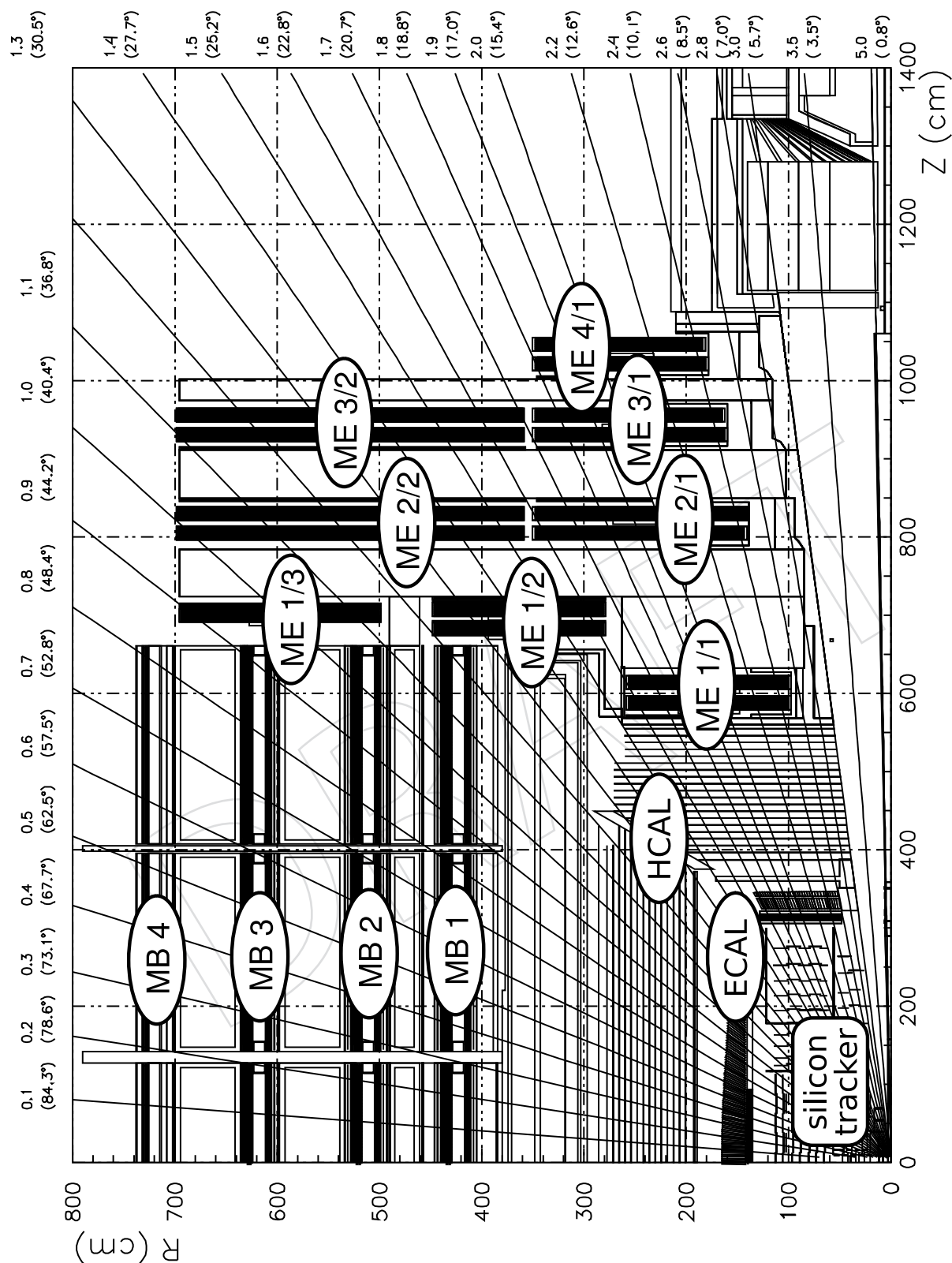


Figure 1: A quarter-view of CMS with labeled muon barrel (MB) and endcap (ME) stations.

3). Endcap CSCs contain 6 identical layers, each of which measures both coordinates with intersecting cathode strips and anode wires.

1.2 Coordinate systems and conventions

The global CMS coordinate system is defined by the inner silicon tracker, which is aligned relative to the LHC beamline and interaction point. The $+z$ direction points along the beamline, to the west. The $+y$ axis points vertically upward, with $+x$ forming a right-handed coordinate system by pointing south [2]. The origin is the average position of tracker elements, close to the interaction point [3]. These same coordinates can be expressed cylindrically, with x and y replaced by $r = \sqrt{x^2 + y^2}$ and $\phi = \text{atan2}(y, x)$. The curvilinear coordinate $r\phi$ is perpendicular to the beamline and rays from the beamline, and differentials of $r\phi$ are understood to vary in ϕ , not r (so $d(r\phi)$ is equivalent to $r d\phi$).

Each muon chamber and layer has its own local coordinate system, centered on the subdetector with local z being perpendicular to the measurement planes, and $+z$ points in the direction of decreasing layer number. The local x axis roughly corresponds to global $r\phi$, and local y forms a right-handed coordinate system. In the absence of misalignment, y is parallel to the beamline for DT chambers and radial for CSCs.

Layer/superlayer coordinate systems differ slightly from their parent chambers. The origin of each coordinate system is centered such that $z = 0$ lies on the layer, and DT superlayers have small offsets in x as well. The middle superlayer of DT chambers are rotated 90° with respect to the chamber coordinates, such that x measurements in these layers are y positions in chamber coordinates. Internal alignments of layers introduce additional corrections.

Cathode strips in CSCs fan radially from the beamline, intersected by anode wires. The strips measure a coordinate perpendicular to their orientation, which in the absence of misalignment coincides with global $r\phi$ throughout the chamber. We find “local $r\phi$,” or local x times the cosine of the strip angle, to be a more convenient coordinate than x for CSCs.

We describe the orientations of chambers and layers with ϕ_x , ϕ_y , and ϕ_z , where each is a right-hand rotation around the corresponding coordinate axis. The 3-D rotation is the following right-to-left composition:

$$\begin{pmatrix} 1 & 0 & 0 \\ 0 & \cos \phi_x & \sin \phi_x \\ 0 & -\sin \phi_x & \cos \phi_x \end{pmatrix} \cdot \begin{pmatrix} \cos \phi_y & 0 & -\sin \phi_y \\ 0 & 1 & 0 \\ \sin \phi_y & 0 & \cos \phi_y \end{pmatrix} \cdot \begin{pmatrix} \cos \phi_z & \sin \phi_z & 0 \\ -\sin \phi_z & \cos \phi_z & 0 \\ 0 & 0 & 1 \end{pmatrix} \quad (1)$$

2 DT Internal Alignment

This section describes the alignment of layers and superlayers within DT chambers, using local information only. Tracking data are combined with physical measurements performed when the chambers were constructed to resolve ambiguities that would be faced by tracks alone. The chamber geometry obtained by these methods is an important part of the global alignment described in a later section.

2.1 Algorithm for General DT Layer Alignment

The tracks and physical survey data were merged into a consistent geometry with a method based on the MillePede algorithm of V. Blobel [4]. The basic idea behind this algorithm is to define a χ^2 with contributions from all sources: alignment, track residuals, and survey residuals, and then minimize the χ^2 , allowing all parameters to float.

Alignment corrections are represented by a vector with 6 parameters per alignable (layers, superlayers, and in a later section, the chambers themselves). These are $\delta_x^i, \delta_y^i, \delta_z^i, \delta_{\phi_x}^i, \delta_{\phi_y}^i$, and $\delta_{\phi_z}^i$ with i indexing the alignables. Varying the alignment affects residuals, the difference between hits and track fits. Layers and superlayers measure hit positions in only one dimension, so the effect of geometric corrections on residuals (Δx_j^{geom} on alignable i and track j) can be related to alignment parameters through the following matrix:

$$\begin{pmatrix} \Delta x_j^{\text{geom}} \end{pmatrix} = \begin{pmatrix} -1 & 0 & \frac{dx}{dz} & -y \frac{dx}{dz} & x \frac{dx}{dz} & -y \end{pmatrix} \cdot \begin{pmatrix} \delta_x^i \\ \delta_y^i \\ \delta_z^i \\ \delta_{\phi_x}^i \\ \delta_{\phi_y}^i \\ \delta_{\phi_z}^i \end{pmatrix} \quad (2)$$

for each alignable (where y and $\frac{dx}{dz}$ are the track's y position and x slope with respect to z , in the layer's coordinate system). Tracks are most sensitive to δ_x , and they have no sensitivity to δ_y because the term connecting it to Δx^{geom} is zero. We will henceforth denote the vector of all alignment parameters as $\vec{\delta}$, and the matrix connecting them to Δx^{geom} as A (the index i is internal). Expanding equation 2 to cover all alignables,

$$\begin{pmatrix} \Delta x_j^{\text{geom}} \end{pmatrix} = A \cdot \vec{\delta}. \quad (3)$$

Track-fitting is part of the global minimization, so we must include a term corresponding to variation the track parameters. We parameterize tracks inside of DT chambers as straight lines ($x_0, y_0, \frac{dx}{dz}$ and $\frac{dy}{dz}$), since magnetic field lines mainly follow the yokes between chambers, leaving negligible magnetic field in the chambers themselves. The effect of small corrections in the track parameters on residuals $\Delta x_j^{\text{track}}$ is also linear, and may be represented by a matrix multiplying the track parameter corrections

$$\begin{pmatrix} \Delta x_j^{\text{track}} \\ \Delta y_j^{\text{track}} \end{pmatrix} = \begin{pmatrix} 1 & 0 & z_i & 0 \\ 0 & 1 & 0 & z_i \end{pmatrix} \cdot \begin{pmatrix} \delta_{x_0j} \\ \delta_{y_0j} \\ \delta_{\frac{dx}{dz}j} \\ \delta_{\frac{dy}{dz}j} \end{pmatrix} \quad (4)$$

in the chamber's coordinate system. (As a reminder, one-dimensional Δx residuals in layer coordinates transform to $(\Delta x, 0)$ in chamber coordinates for outer superlayers and $(0, \Delta y)$ for the middle superlayer, in the absence of alignment corrections.) We will denote the corrections to the track parameters as $\delta \vec{p}_j$ and the matrix connecting them to x^{track} as B_j , such that Equation 4 becomes

$$\begin{pmatrix} \Delta x_j^{\text{track}} \\ \Delta y_j^{\text{track}} \end{pmatrix} = B_j \cdot \delta \vec{p}_j. \quad (5)$$

The observed residuals $\Delta \vec{x}$ are

$$\Delta \vec{x} = \Delta \vec{x}^{\text{geom}} + \Delta \vec{x}^{\text{track}} + \Delta \vec{x}^{\text{meas}} \quad (6)$$

where $\Delta \vec{x}^{\text{meas}}$ is a random contribution from measurement error, assumed to be symmetric. We can now construct a χ^2 which is minimized when tracks and chamber geometry are mutually

consistent:

$$\chi^2_{\text{track-based}} = \sum_j \left(\Delta \vec{x} - A \cdot \vec{\delta} - B_j \cdot \delta \vec{p}_j \right)^T (\sigma_{\text{resid}}^2)^{-1} \left(\Delta \vec{x} - A \cdot \vec{\delta} - B_j \cdot \delta \vec{p}_j \right) \quad (7)$$

where σ_{resid}^2 is the covariance matrix of hits (no uncertainty in our track model). However, $\chi^2_{\text{track-based}}$ cannot be minimized because the matrix of its derivatives is singular: the system has more degrees of freedom than constraints. We therefore must augment it with external data to yield a meaningful alignment.

2.1.1 Quality Control Measurements

As the DT chambers were being built, the positions of the wire end-pins were measured and recorded [5]. Local δ_x^i corrections can be determined from an average of the measurements over layers. Typical (RMS) corrections are 100 μm , with an uncertainty of 30–40 μm . These measurements only constrain the relative positions of layers within each superlayer, not the superlayers relative to one another, because each superlayer was built separately.

2.1.2 Photogrammetry Measurements

After superlayers were assembled into chambers, the position and orientation of the superlayers were measured by photogrammetry (a photograph of reflective targets at known points on the superlayer, in a coordinate system defined by references at their corners [6]). These measurements constrain superlayers relative to one another, but not the layers inside).

Typical corrections are 200 μm for δ_x and δ_y , with 150 μrad for rotations. The δ_z corrections were 1–1.5 mm because of a layer of glue not included in the design description. We take special care to cross-check these δ_z parameters independently with tracks before applying the correction.

2.1.3 Combination

To include survey measurements into the global alignment fit, we need a term to describe the effect of alignment corrections $\vec{\delta}^i$ on the positions of the survey's control points (nominally at x_k, y_k, z_k). This term is

$$\Delta \vec{x}_k^{\text{points}} = \begin{pmatrix} 1 & 0 & 0 & y_k & z_k & 0 \\ 0 & 1 & 0 & -x_k & 0 & z_k \\ 0 & 0 & 1 & 0 & -x_k & -y_k \end{pmatrix} \cdot \vec{\delta}^i \quad (8)$$

and we denote the matrix for all control points on all alignables as C (alignable index i and survey point index k are internal). This matrix internally accounts for the fact that some measurements are relative differences, rather than absolute coordinates. The χ^2 of survey measurements is

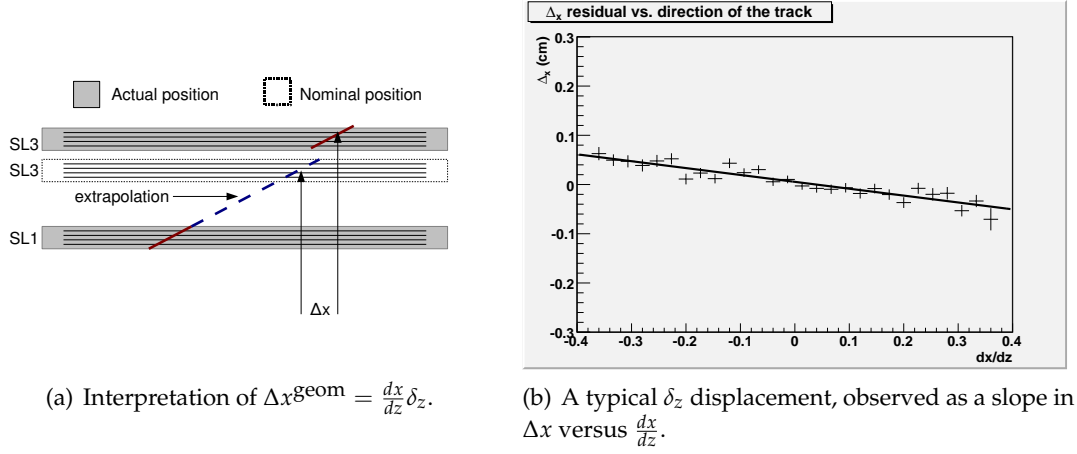
$$\chi^2_{\text{survey}} = \left(\Delta \vec{x}^{\text{survey}} - C \cdot \vec{\delta} \right)^T (\sigma_{\text{survey}}^2)^{-1} \left(\Delta \vec{x}^{\text{survey}} - C \cdot \vec{\delta} \right) \quad (9)$$

where $\Delta \vec{x}^{\text{survey}}$ are the measured positions from survey and photogrammetry, and σ_{survey}^2 is their covariance matrix.

Finally, the global chamber position can never be determined from local information, so translations and rotations of the whole chamber are fixed to zero with Lagrange multipliers $f(\lambda)$. The final χ^2 is

$$\chi^2 = \chi^2_{\text{track-based}} + \chi^2_{\text{survey}} + f(\lambda), \quad (10)$$

which we minimize by a straight-forward numerical inversion of the derivatives matrix, as the number of alignable parameters is not large.

Figure 2: Measuring δ_z with tracks only.

2.2 Independent Cross-Check of δ_z

As explained above, the largest correction from the design geometry was in the superlayers' z coordinates, due to a layer of glue not included in the design description. To cross-check these photogrammetry measurements, we determined them from an independent track-based measurement.

As the displacement under study is between superlayers, track segments fitted in each superlayer individually are not affected by the correction. We can therefore simplify the χ^2 by re-defining residuals in this case as a difference between single-superlayer track segments (superlayers 1 and 3 only), extrapolated to a common plane. The B_j matrix vanishes, leaving us with

$$\chi^2 = \sum_j \left(\Delta \vec{x} - A \cdot \vec{\delta} \right)^T (\sigma_{\text{resid}}^2)^{-1} \left(\Delta \vec{x} - A \cdot \vec{\delta} \right) \quad (11)$$

where σ_{resid}^2 is the covariance matrix for these new residuals. We further simplify the alignment by only allowing δ_x , δ_z , and δ_{ϕ_y} to float, as these are the parameters that can be determined purely from track segments in 1-dimensional measurement devices. The alignment derivatives matrix A for each chamber is reduced to

$$\left(\Delta x_j^{i \text{ geom}} \right) = \begin{pmatrix} -1 & \frac{dx}{dz} & x \frac{dx}{dz} \end{pmatrix} \cdot \begin{pmatrix} \delta_x^i \\ \delta_z^i \\ \delta_{\phi_y}^i \end{pmatrix}. \quad (12)$$

A geometric interpretation of the δ_z term is given in Figure 2.

The δ_z corrections from survey (photogrammetry), this track-based method, and their differences are plotted in Figure 3, revealing independent agreement in non-negligible corrections. Typical discrepancies are $580 \mu\text{m}$ (RMS and Gaussian width) in δ_z , while the size of the corrections range from 1 to 2 mm (thicker glue was used in station 1). The δ_x and δ_{ϕ_y} corrections were also in agreement, but they were negligible ($80 \mu\text{m}$ and $50 \mu\text{mrad}$, respectively).

The internal DT geometry used in the global alignment was determined by the combined fit described in subsection 2.1 with δ_z fixed, followed by corrections from the tracks-only method described above. It therefore incorporates all available information except that which is reserved for cross-checking the sources.

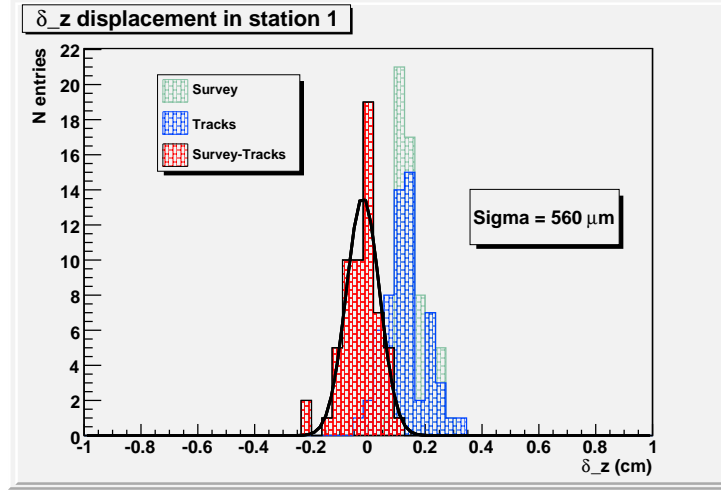


Figure 3: Comparison of survey and track-based alignment of δ_z .

3 CSC Overlaps Alignment

The CSCs in the muon endcap were designed to overlap slightly along their edges, such that a track passing through the narrow “overlap regions” would be observed by both of the neighboring chambers, without scattering volumes in between or propagation over long distances. These tracks can therefore measure the relative alignment of the pairs of chambers they connect with high precision. All endcap rings except for ME1/3 are connected in this way by overlaps. In this section, we will describe a method to align CSCs within each ring with only a small sample of tracks and demonstrate the accuracy of the method by comparing its results with an independent measurement.

3.1 Algorithm

The basic strategy is to measure differences in alignment parameters for pairs of chambers and then propagate alignment corrections around the ring by solving a system of equations. Relative alignment corrections between neighboring chambers i and $i + 1$ are derived from the consistency of track segments with a single, straight line.

At each interface between two chambers, we fit hits in the 6 layers of each chamber to straight lines $r\phi_i(z) = a_i + b_i z$ and $r\phi_{i+1}(z) = a_{i+1} + b_{i+1} z$ in a shared coordinate system and then propagate these segments to a plane equidistant between the two chambers (at $z = 0$). The position-matching residual on the plane is $\Delta a = a_i - a_{i+1}$ and the angle-matching residual is $\Delta b = b_i - b_{i+1}$. The overlap region is a thin strip spanning the chamber only along the y dimension, so we can consider fitting these residuals as a function of the track’s y intersection with the plane of comparison. We therefore have access to four types of residuals:

- $\Delta a(y)$ intercept at $y = 0$: the relative $\delta_{r\phi}$ correction in position along a circle centered on the beamline,
- $\Delta b(y)$ intercept at $y = 0$: the relative δ_{ϕ_y} angle between the two chambers,
- $\Delta a(y)$ slope: the relative δ_{ϕ_z} angle,
- $\Delta b(y)$ slope: a non-rigid twist of the chambers.

We consider only the three alignment corrections, presented graphically in Fig. 4.

While it is possible to resolve all three corrections at once, note that δ_{ϕ_y} is independent of the

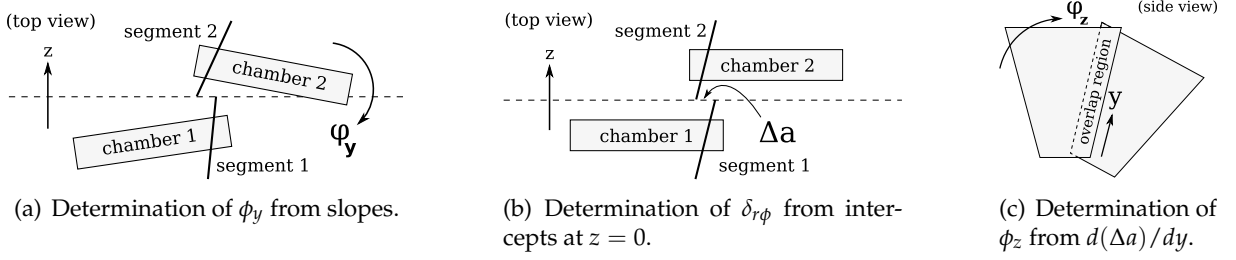


Figure 4: The three alignment parameters accessible to local track matching in CSCs.

other two and $\delta_{r\phi}$ is independent of δ_{ϕ_z} . We can therefore ignore dependencies if we align the parameters in the following order: δ_{ϕ_y} , then $\delta_{r\phi}$, and then δ_{ϕ_z} .

The problem of propagating alignment corrections around the ring is identical for each of the three parameters, so we will present it only once in an abstract way. Label the mean of each residuals distribution $\alpha_{i,i+1}$ (for each of the three types of residuals under consideration) with A_i and A_{i+1} being the alignment corrections for the neighboring chambers (δ_{ϕ_y} , $\delta_{r\phi}$, or δ_{ϕ_z}). Each ring has $N = 18$ or 36 chambers, so i ranges from 1 to N with the convention that $N + 1 = 1$ (to close the loop).

If we move chamber i and $i + 1$ by A_i and A_{i+1} , the mean of the residuals between them can be expected to change by $(A_i - A_{i+1})$. To optimize all of the residuals at once, we define a χ^2 as

$$\chi^2 = (\alpha_{12} - A_1 + A_2)^2 + (\alpha_{23} - A_2 + A_3)^2 + \dots + (\alpha_{N1} - A_N + A_1)^2 \quad (13)$$

and minimize it by setting its derivatives to zero. For example,

$$\frac{1}{2} \frac{\partial \chi^2}{\partial A_2} = (\alpha_{12} - A_1 + A_2) - (\alpha_{23} - A_2 + A_3) = 0. \quad (14)$$

A complete set of such equations, written in matrix form, looks like the following (with $N = 5$ for brevity):

$$\begin{pmatrix} \alpha_{12} - \alpha_{51} \\ \alpha_{23} - \alpha_{12} \\ \alpha_{34} - \alpha_{23} \\ \alpha_{45} - \alpha_{34} \\ \alpha_{51} - \alpha_{45} \end{pmatrix} = \begin{pmatrix} 2 & -1 & & & -1 \\ -1 & 2 & -1 & & \\ & -1 & 2 & -1 & \\ & & -1 & 2 & -1 \\ -1 & & & -1 & 2 \end{pmatrix} \begin{pmatrix} A_1 \\ A_2 \\ A_3 \\ A_4 \\ A_5 \end{pmatrix}. \quad (15)$$

To align all N chambers, we need only invert this $N \times N$ matrix, and N is small enough to be manageable.

Unfortunately, the matrix in Equation 15 is singular because a relative alignment procedure cannot determine the global position of the whole system. Rotating the whole ring rigidly by adding the same constant to every A_i would leave the χ^2 invariant. This is a flat direction in (A_1, A_2, \dots, A_N) space, and it can be unflattened by preferring the corrections A_i to be as small as possible. We add the average of A_i

$$\left[\frac{1}{N} (A_1 + A_2 + \dots + A_N) \right]^2 \quad (16)$$

to the χ^2 so that it will be minimized, and each derivative equation becomes

$$\frac{1}{2} \frac{\partial \chi^2}{\partial A_i} = (\alpha_{i-1,i} - A_{i-1} + A_i) - (\alpha_{i,i+1} - A_i + A_{i+1}) + \frac{1}{N^2} \sum_{i=1}^N A_i = 0. \quad (17)$$

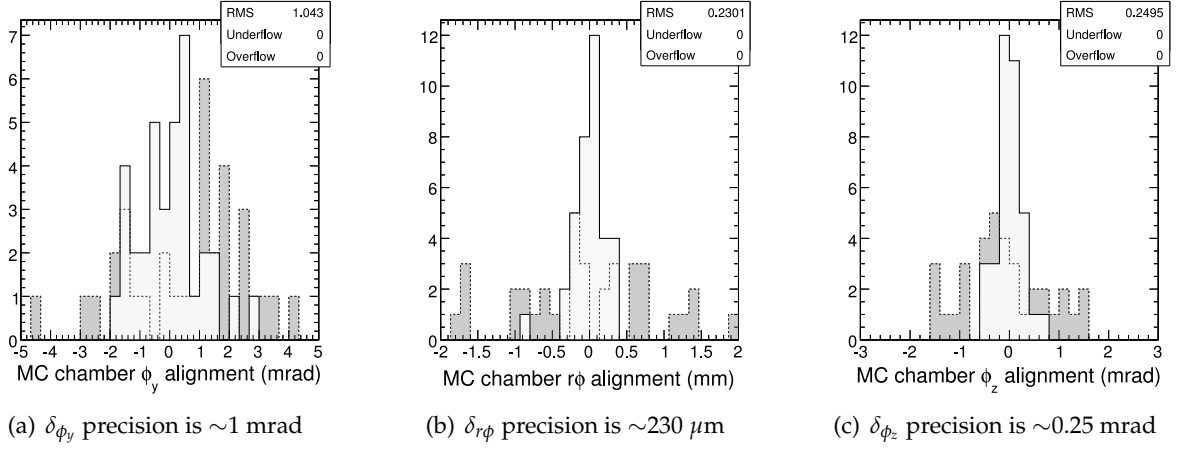


Figure 5: Comparison of alignment parameters with MC truth before (dark) and after (light) a simulated beam-halo alignment with similar statistics to the 2008 LHC run.

The matrix equation is now

$$\begin{pmatrix} \alpha_{12} - \alpha_{51} \\ \alpha_{23} - \alpha_{12} \\ \alpha_{34} - \alpha_{23} \\ \alpha_{45} - \alpha_{34} \\ \alpha_{51} - \alpha_{45} \end{pmatrix} = \begin{bmatrix} \begin{pmatrix} 2 & -1 & & & -1 \\ -1 & 2 & -1 & & \\ & -1 & 2 & -1 & \\ & & -1 & 2 & -1 \\ -1 & & & -1 & 2 \end{pmatrix} + \frac{1}{N^2} \begin{pmatrix} 1 & 1 & 1 & 1 & 1 \\ 1 & 1 & 1 & 1 & 1 \\ 1 & 1 & 1 & 1 & 1 \\ 1 & 1 & 1 & 1 & 1 \\ 1 & 1 & 1 & 1 & 1 \end{pmatrix} \end{bmatrix} \begin{pmatrix} A_1 \\ A_2 \\ A_3 \\ A_4 \\ A_5 \end{pmatrix}. \quad (18)$$

155 It has a unique solution in which the average of A_i is exactly zero.

The circular ring of chambers also provides an internal cross-check: the closure

$$\sum_{i=1}^N \alpha_{i,i+1} - (A_i - A_{i+1}) = \sum_{i=1}^N \alpha_{i,i+1} \quad (19)$$

156 must be zero. The closure is independent of alignment, because all A_i terms cancel in the sum.
 157 A non-zero closure would indicate an incorrect circumference for the ring, either from our
 158 description of the chamber widths or their radial distance from the beamline. All measured
 159 values of closure were consistent with zero.

160 This algorithm can be extended to align layers within the CSC chambers, taking advantage
 161 of the two-chamber overlap to resolve ambiguities between track-fitting and layer alignment
 162 in an isolated chamber. In the 2008 LHC beam-halo run, many layer measurements were not
 163 statistically significant, with a precision of $50\text{--}100 \mu\text{m}$, so we do not present the results here.

164 3.2 Monte Carlo Studies

165 The procedure was first applied to beam-halo Monte Carlo with approximately the same num-
 166 ber of events as the 2008 LHC run. The azimuthal and radial distributions are not exactly the
 167 same as in data, as they are notoriously difficult to predict for a new accelerator. Starting from
 168 a misaligned detector, the procedure re-aligned $\delta\phi_y$ with about 1 mrad precision, δr_ϕ with about
 169 $230 \mu\text{m}$, and $\delta\phi_z$ with about 0.25 mrad, by comparison with the true positions of the chambers,
 170 known in simulation (MC-truth). Fig. 5 shows histograms of the differences between aligned
 171 values of the parameters and MC-truth.

3.3 Alignment Results

At about 11:50 PM on September 11, 2008, protons circulated in beam-2 of the LHC tunnel for 9 minutes (CMS run 60232), enough to test the CSC Overlaps procedure. The inner ring (ring 1) of each disk was more illuminated because beam-halo muons tend to fly close to the beamline. At that time, all chambers in ME-2/1 and ME-3/1 were operational, so we aligned these chambers with the CSC Overlaps algorithm.

To verify the aligned positions, we compare them with photogrammetry, an alignment derived from a literal photograph of the detector. Each chamber has two reflective alignment pins whose positions can be measured with $300\ \mu\text{m}$ precision by photographing them in a strong light. From these, $\delta_{r\phi}$ and δ_{ϕ_z} corrections (relative to the design geometry) can be computed with $(300\ \mu\text{m})/\sqrt{2} = 210\ \mu\text{m}$ and $(300\ \mu\text{m}) \cdot \sqrt{2}/1.85\ \text{m} = 0.23\ \text{mrad}$ precision, respectively. Though photogrammetry is only valid before chambers are physically moved by the magnetic field, it is completely independent from the track-based alignment that can be derived with the field on or off.

In Figure 6, the track-based and photogrammetry corrections to ideal geometry are presented. Both yield significant deviations from zero, yet agree rather well. We plot the same data as histograms of differences between track-based and photogrammetry measurements in Figure 7, and observe that the widths of these distributions are $340\ \mu\text{m}$ and $0.42\ \text{mrad}$. Subtracting the photogrammetry uncertainties in quadrature from standard deviations observed in the plots,

$$\text{track-based } \delta_{r\phi} \text{ accuracy} = \sqrt{(340\ \mu\text{m})^2 - (210\ \mu\text{m})^2} = 270\ \mu\text{m} \quad (20)$$

$$\text{track-based } \phi_z \text{ accuracy} = \sqrt{(0.42\ \text{mrad})^2 - (0.23\ \text{mrad})^2} = 0.35\ \text{mrad}, \quad (21)$$

in rough agreement with the Monte Carlo prediction and close to the $116\ \mu\text{m}$ intrinsic hit resolution of the detectors. Assuming that the errors are statistical, 25 minutes or more of similar tracks would yield an alignment that is more precise than the hits themselves.

4 Global Muon Alignment

Local muon alignment procedures arrange sets of chambers in self-consistent coordinate systems, but cannot relate those coordinates to the locations of other subsystems of CMS, particularly the inner silicon tracker. In this section, we describe methods to align muon chambers relative to the silicon tracker, such that all tracking volumes in CMS share one global system of coordinates. Since these global alignment methods are independent of the local alignments, they can be used to cross-check each other.

Two algorithms, HIP (Hits and Impact Points) and MillePede, have been developed to align muon chambers relative to the tracker. Each is described in its own section below, followed by Monte Carlo and systematics studies of both, and then results of each with cosmic ray data.

4.1 The HIP Algorithm

The basic idea of the HIP algorithm is to accumulate high- p_T muons which pass through two regions: a well-aligned “reference” volume, usually the silicon tracker, and the “target” volume under study. Muon tracks are fitted using information from the reference only, and chambers in the target are translated and rotated to minimize the distance between muon hits and the impact points (intersections) of tracks on the layer planes.

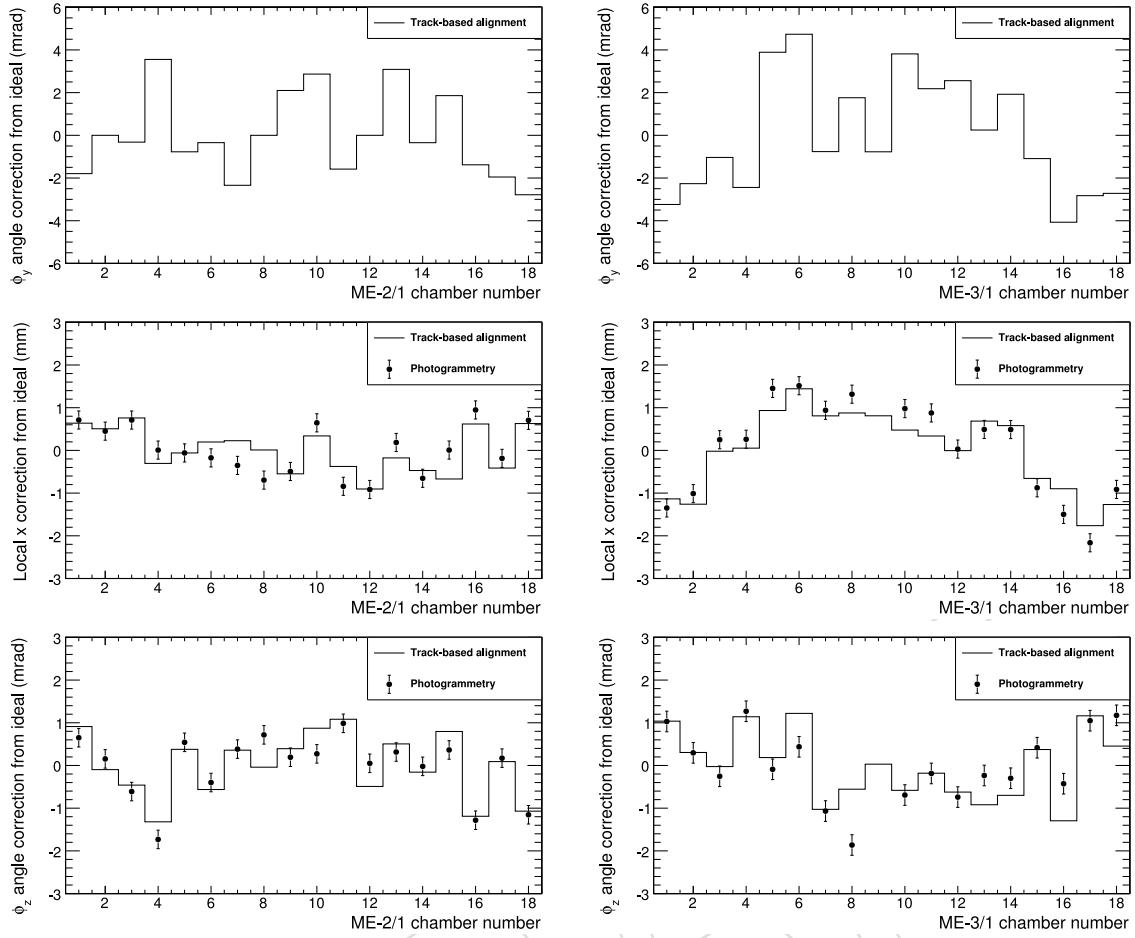


Figure 6: CSC alignment results from the Overlaps procedure and the 2008 LHC run, presented as a difference from ideal and compared with photogrammetry where possible.

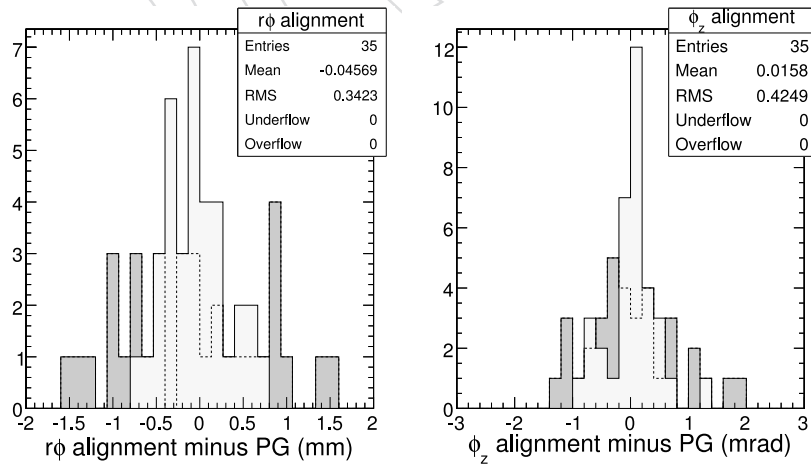


Figure 7: Chamber-by-chamber verification of the beam-halo alignment with photogrammetry. The dark histogram is before alignment; the light histogram and statistics box are after alignment.

Between each consecutive chamber along a muon's path are thick (20–60 cm) layers of iron used as a return yoke for the CMS solenoid. In the iron, magnetic fields are stronger and probabilities are higher that the muon's trajectory will multiply or abruptly scatter, making its direction less predictable than when it passes through the gas volumes of the chambers themselves. It is therefore appropriate to combine hits in each chamber, such that one chamber yields one independent measurement per track.

The hits in each chamber are combined into four observables, Δx , Δy , $\Delta \frac{dx}{dz}$, and $\Delta \frac{dy}{dz}$, which are the differences between the track's 2-D location and entrance angle, respectively, with the pattern of hits in the chamber. We compute these observables by fitting raw residuals to a straight line as a function of the local z positions of the layers. The reduced χ^2 of the linear fit to residuals expresses the quality of the measurement (independent of the distance between the track and the hits), so we use N_{dof}/χ^2 as a weight in the final alignment. Station 4 DT chambers can only measure one dimension, so they observe only Δx and $\Delta \frac{dx}{dz}$, and strip measurements in CSCs observe $\Delta r\phi$ and $\Delta d(r\phi)/dz$.

Residuals between target hits and tracks propagated from the reference track-fitting volume are influenced by four categories of effects:

- misalignment of the target chamber (geometric residuals),
- statistical uncertainty in the track fit,
- propagation errors from multiple (Gaussian) and single (power-law) scattering,
- biases in the track source or chamber itself.

Our goal is to identify errors of the first category, though the first three are convoluted together in a statistical distribution, and the fourth can only be diagnosed by an independent method (such as local alignment techniques described in the previous sections).

Assuming that we can isolate geometric residuals Δx^{geom} , Δy^{geom} , $\Delta \frac{dx}{dz}^{\text{geom}}$, and $\Delta \frac{dy}{dz}^{\text{geom}}$, the alignment corrections δ_x , δ_y , δ_z , δ_{ϕ_x} , δ_{ϕ_y} , and δ_{ϕ_z} can be computed by solving the following:

$$\begin{pmatrix} \Delta x^{\text{geom}} \\ \Delta y^{\text{geom}} \\ \Delta \frac{dx}{dz}^{\text{geom}} \\ \Delta \frac{dy}{dz}^{\text{geom}} \end{pmatrix} = \begin{pmatrix} 1 & 0 & -\frac{dx}{dz} & -y\frac{dx}{dz} & x\frac{dx}{dz} & -y \\ 0 & 1 & -\frac{dy}{dz} & -y\frac{dy}{dz} & x\frac{dy}{dz} & x \\ 0 & 0 & 0 & -\frac{dx}{dz}\frac{dy}{dz} & 1 + \left(\frac{dx}{dz}\right)^2 & -\frac{dy}{dz} \\ 0 & 0 & 0 & -1 - \left(\frac{dy}{dz}\right)^2 & \frac{dx}{dz}\frac{dy}{dz} & \frac{dx}{dz} \end{pmatrix} \begin{pmatrix} \delta_x \\ \delta_y \\ \delta_z \\ \delta_{\phi_x} \\ \delta_{\phi_y} \\ \delta_{\phi_z} \end{pmatrix}. \quad (22)$$

For CSCs, the curvilinear residuals $\Delta r\phi^{\text{geom}}$ and $\Delta d(r\phi)/dz^{\text{geom}}$ introduce corrections suppressed by r , the radial distance to the beamline:

$$\begin{pmatrix} \Delta r\phi^{\text{geom}} \\ \Delta \frac{dr\phi}{dz}^{\text{geom}} \end{pmatrix} = \begin{pmatrix} 1 & \left[-\frac{x}{r} + 3\left(\frac{x}{r}\right)^3\right] & -\frac{dx}{dz} & -y\frac{dx}{dz} & x\frac{dx}{dz} & -y \\ 0 & -\frac{dx}{dz}\left(\frac{1}{2r}\right) & 0 & \left[\frac{x}{r} - \frac{dx}{dz}\frac{dy}{dz}\right] & 1 + \left(\frac{dx}{dz}\right)^2 & -\frac{dy}{dz} \end{pmatrix} \begin{pmatrix} \delta_x \\ \delta_y \\ \delta_z \\ \delta_{\phi_x} \\ \delta_{\phi_y} \\ \delta_{\phi_z} \end{pmatrix}. \quad (23)$$

To extract geometric residuals from the measurements, we construct an ansatz describing all effects and fit it to the data. Each of the four observables is represented by a convolution of a Gaussian and a Lorentzian (to model the power-law scattering tails),

$$f(t; t_0, \sigma, \gamma) = \int_{-\infty}^{\infty} \frac{1}{\pi} \frac{\gamma}{(t-s-t_0)^2 + (\gamma)^2} \times \frac{1}{\sqrt{2\pi}\sigma} \exp\left(\frac{-s^2}{2\sigma^2}\right) ds. \quad (24)$$

Position residuals are correlated with their corresponding angle residuals because any error in the propagated track's direction upstream of the chamber grows in both angle and position. Therefore, a 2-D distribution of Δx and $\Delta \frac{dx}{dz}$ is skewed by a parameter $\alpha_{\Delta x}$:

$$f\left(\Delta x; (\Delta x_0 + \alpha_{\Delta x} \Delta \frac{dx}{dz}), \sigma_{\Delta x}, \gamma_{\Delta x}\right) \times f\left(\Delta \frac{dx}{dz}; \Delta \frac{dx}{dz}_0, \sigma_{\Delta \frac{dx}{dz}}, \gamma_{\Delta \frac{dx}{dz}}\right) \quad (25)$$

The peak of the complete 4-D distribution in $(\Delta x, \Delta y, \Delta \frac{dx}{dz}, \Delta \frac{dy}{dz})$ space is the left-hand-side of Equation 22, because the geometric effect on residuals can be thought of as a 4-D delta distribution, and it must be convoluted with the Gaussian and Lorentzian (to integrate out $\Delta x_0, \Delta y_0, \Delta \frac{dx}{dz}_0$ and $\Delta \frac{dy}{dz}_0$). This introduces a dependence of our complete fit function on the alignment corrections ($\delta_x, \delta_y, \delta_z, \delta_{\phi_x}, \delta_{\phi_y}$, and δ_{ϕ_z}) as fit parameters, and the track impact point (x, y) and entrance angle $(\frac{dx}{dz}, \frac{dy}{dz})$ as dimensions in the data space. In total, the fit function has 16 parameters and 8 dimensions for DT stations 1–3, 11 parameters and 6 dimensions for CSCs, and 10 parameters, 6 dimensions for DT station 4 (no access to δ_y). The most relevant projections of an example fit are shown in Figure 8. The fit is performed by MINUIT [7] with an unbinned maximum likelihood method, using the weights described above.

If the magnetic field or material maps are not perfectly represented in track propagation, residuals will be biased as an antisymmetric function of track curvature, q/p_T . To correct for any such errors, we split the sample into two bins, one for each charge q , and perform the alignment separately in each bin. Muons and antimuons have the same spectral distribution in cosmic rays (though not the same flux), so a simple average of $q < 0$ and $q > 0$ results cancels the antisymmetric bias in all alignment corrections except δ_z . The difference of the two bins is maximally sensitive to the bias and can be used to measure it.

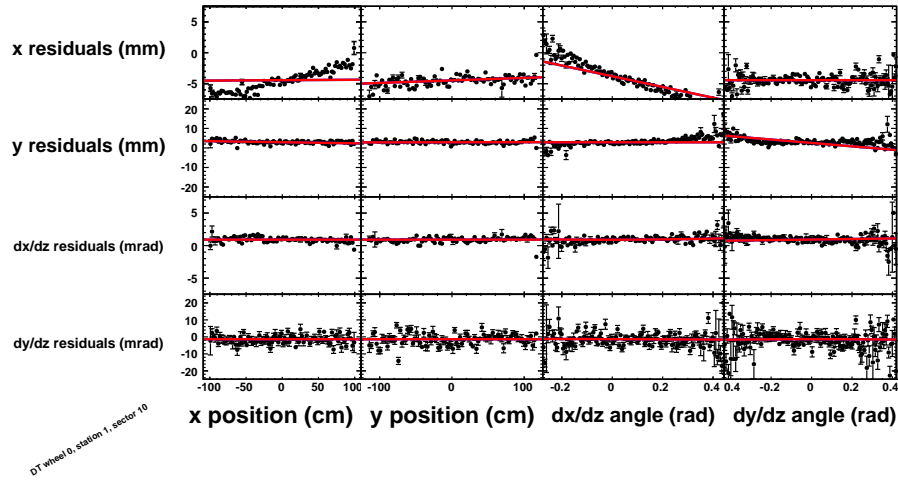
Repeated applications of the procedure converge quickly to an optimal solution. Significant corrections are only observed in the first and second iterations (in data and Monte Carlo), so we always perform three iterations.

4.2 The MilliPede Algorithm

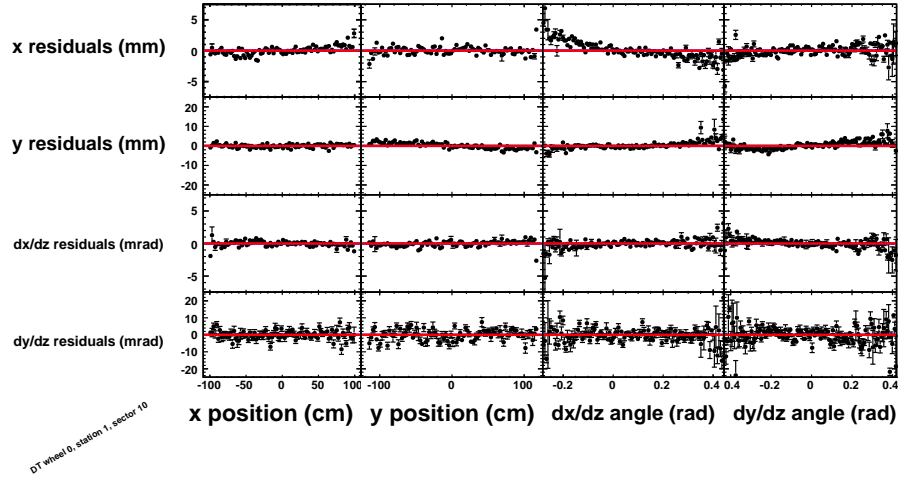
The Millepede algorithm implemented for the muon system is a particular case of the most general Millepede algorithm ?? by V. Blobel. The basic idea is to perform a minimization of the residuals (difference between the hit and the track intersection with the current detector plane) against the alignment and track parameters together in the same fit.

Nevertheless, for the muon system the tracker track is assumed to be perfect and track parameters in the fit are fixed to the tracker track estimation. This constrain distangles the muon system in the fit allowing an individual treatment of each detector plane in a collection of simpler fits which only take into account the alignment parameters of the considered detector.

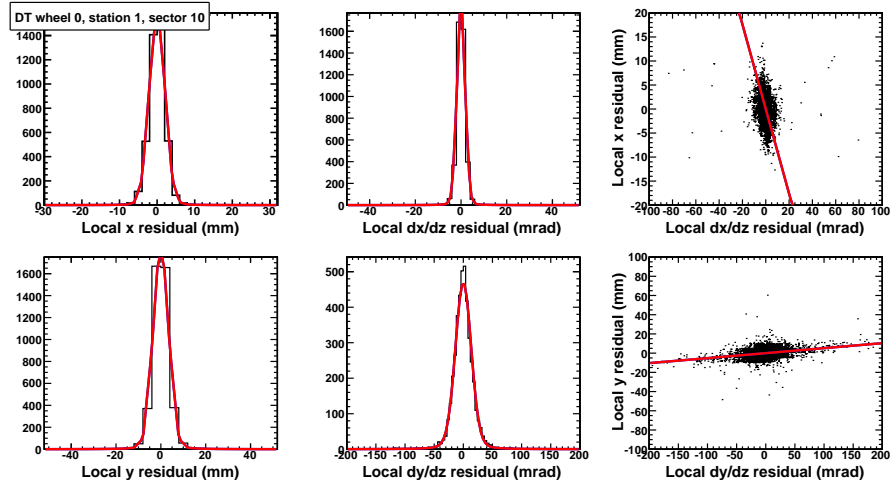
The chamber is the minimum alignment unit considered by the Millepede algorithm. The motivation for this comes from the fact that chambers in the barrel are separated by almost 1 meter of iron. Scattering processes in the iron could deviate muons in a correlated pattern for



(a) Projection of residuals onto impact point and entrance angle, before alignment.



(b) Projection of residuals onto impact point and entrance angle, after alignment.



(c) Projection of residuals and their correlations, after alignment.

Figure 8: An example fit to cosmic ray data (wheel 0, station 1, sector 10). The red lines are projections of the fit result.

all the hits in a same chamber. A dedicated internal alignment not based on global tracks was described previously in this paper.

The trajectory of the tracks inside the drift tube chambers intersects 12 detecting planes, 8 for the $r\phi$ coordinate and 4 for the θ coordinate. This trajectory is assumed to be locally a straight line and four observables can be extracted: intercept and slope for the ϕ projection (x and $\frac{dx}{dz}$), and intercept and slope for the θ projection (y and $\frac{dy}{dz}$). This is repeated for both the hits and the intersection of the reconstructed track with the detecting planes. Four residuals are defined as the difference between the measurements and the track intersection $\Delta x, \Delta \frac{dx}{dz}, \Delta y, \Delta \frac{dy}{dz}$.

There is a matrix dependency between the residuals and the 6 alignment parameters $\delta_x, \delta_y, \delta_z, \phi_x, \phi_y, \phi_z$, based on a geometrical model and expanded to first order in the alignment parameters.

$$\begin{pmatrix} \Delta x \\ \Delta \frac{dx}{dz} \\ \Delta y \\ \Delta \frac{dy}{dz} \end{pmatrix} = \begin{pmatrix} -1 & 0 & \frac{dx}{dz} & -y \frac{dx}{dz} & x \frac{dx}{dz} & -y \\ 0 & 0 & 0 & \frac{dx}{dz} \frac{dy}{dz} & 1 + \frac{dx}{dz}^2 & -\frac{dy}{dz} \\ 0 & -1 & \frac{dy}{dz} & -y \frac{dy}{dz} & x \frac{dy}{dz} & x \\ 0 & 0 & 0 & -1 - \frac{dx}{dz}^2 & \frac{dx}{dz} \frac{dy}{dz} & \frac{dx}{dz} \end{pmatrix} \cdot \begin{pmatrix} \delta_x \\ \delta_y \\ \delta_z \\ \phi_x \\ \phi_y \\ \phi_z \end{pmatrix} \quad (26)$$

The function to minimize is the following:

$$\chi^2 = \sum_j (\vec{\Delta} - A \vec{\delta})^T E (\vec{\Delta} - A \vec{\delta}) \quad (27)$$

where $\vec{\Delta}$, A and $\vec{\delta}$ are the residual vector, coefficient matrix and alignment parameters vector as described in equation . The E is the inverse of the covariance matrix calculated from the linear fit estimation of the segments. The matrix includes correlations between the position and direction in both projections.

There are several sources of systematic errors affecting to this algorithm:

- DT Calibration. The algorithm uses hits of the DT chambers, which depend on the T0 and tTrig ?? calibrations. Effects resulting from a wrong calibration are absorbed by the method.
- Internal DT alignment. The algorithm assumes all the chambers to behave as perfect rigid bodies. Deformations or misalignments in the internal structure of each chamber might introduce bias in the estimation of the global parameters. In some cases, the algorithm could even compensate for not real effects originated by a wrong internal alignment.
- Multiple Scattering. The multiple scattering of the particles produces large deviations of the track that give place to tails in the residual distributions.
- Magnetic Field. Uncertainties in the description of the magnetic field map introduce systematic effects between the real and the propagated track, which will follow a different path with a different bending.
- Material Budget. Errors in the description of the material crossed by the tracks might cause inconsistencies in the energy loss description, resulting in a bad description of the track.

- Tracker Alignment. The algorithm assumes the tracker track to be perfectly determined. Errors at this level, for example due to a misaligned tracker, are propagated into the muon system, adapting it to the tracker irregularities.

In order to minimize the impact of these systematic errors, several cautions were taken. The algorithm is run over the most up to date DT calibrations and internal DT and tracker geometries. Some of the components of the tracker are not so well aligned due to the poor illumination received by cosmic muons. It is the case of the TEC and the TID. Tracker tracks containing hits from these two subdetectors are discarded. In addition, some restrictions are required to the quality of these tracker tracks. In particular the number of hits in the tracker track is required to be always higher than 15, while the normalized χ^2 must remain below 10. The multiple scattering, material budget and magnetic field bias reduces with the momentum of the muons, for this reason, only muons with $100\text{GeV} < Pt < 200\text{GeV}$ are considered. Finally, to do the calculations as much independent as possible from the tails of the distribution a filtering of the residuals is performed. This is specially important, because in some cases the residual distributions are assymetric. Residual distributions are fitted to a Lorentz function near the peak. The mean and the associated sigma of the fitted function are used to define the region of acceptance of the residuals, which is $[mean - sigma, mean + sigma]$.

4.3 Monte Carlo Study of the Two Algorithms

We tested the algorithms with three Monte Carlo simulations: (1) a geometry-only toy simulation to observe the geometric effects independent of detector effects, (2) a full Pythia and GEANT-based $pp \rightarrow \mu + X$ collisions sample, and (3) a full GEANT-based cosmic ray sample. The sizes of the simulated event samples are all large enough for the alignment results to be systematics-limited, and all detector effects are modelled except tracker misalignment, magnetic field errors, and internal muon chamber misalignment. This demonstrates the alignment reach of the algorithm itself, apart from any possible deficiencies in the input set of tracks.

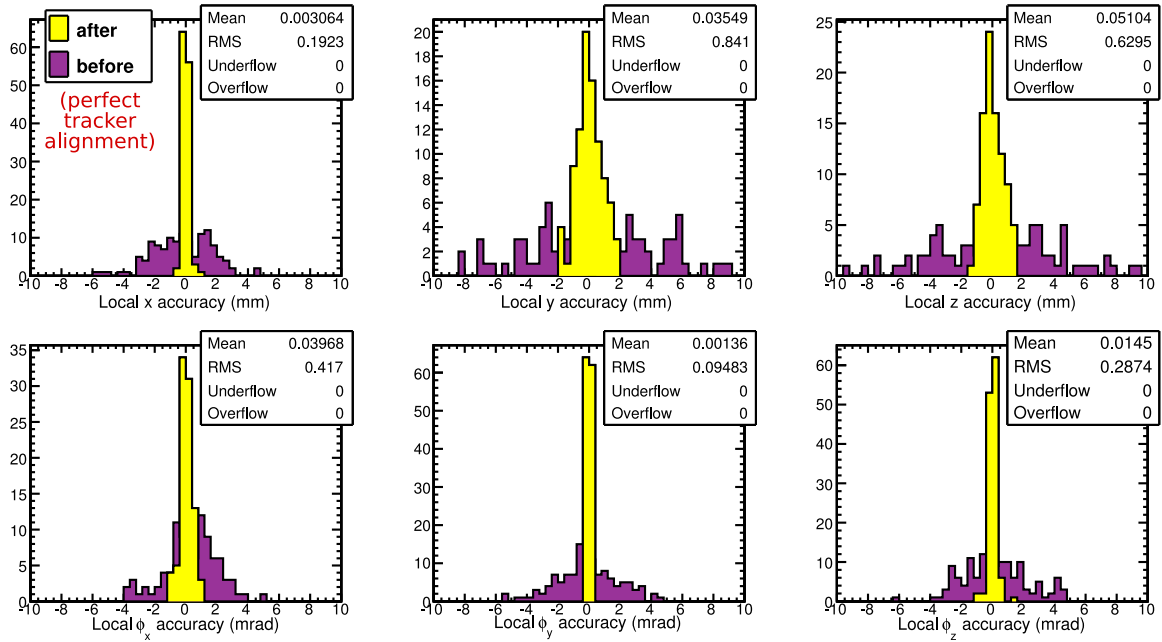
The initial muon system misalignment used in these studies was a Gaussian smearing of chamber positions with 2 mm sigmas in δ_x , 4 mm in δ_y and δ_z , and 2 mrad in the three angles. We then applied each procedure to the simulated events in exactly the same way we do to data. Different initial misalignments yield the same results.

Figure 9 shows differences between aligned positions of each parameter and their true positions for the two algorithms. Interpreting the RMS of these distributions as the alignment accuracy, the δ_x accuracy is 200 μm for HIP, 500 μm for MillePede, close to the intrinsic hit uncertainty of (FIXME: DT hit uncertainty?) for these chambers. Statistical uncertainties returned by the fits are a factor of 3–4 times smaller than the observed accuracy, so this represents the systematic limit of the algorithm as it is currently defined.

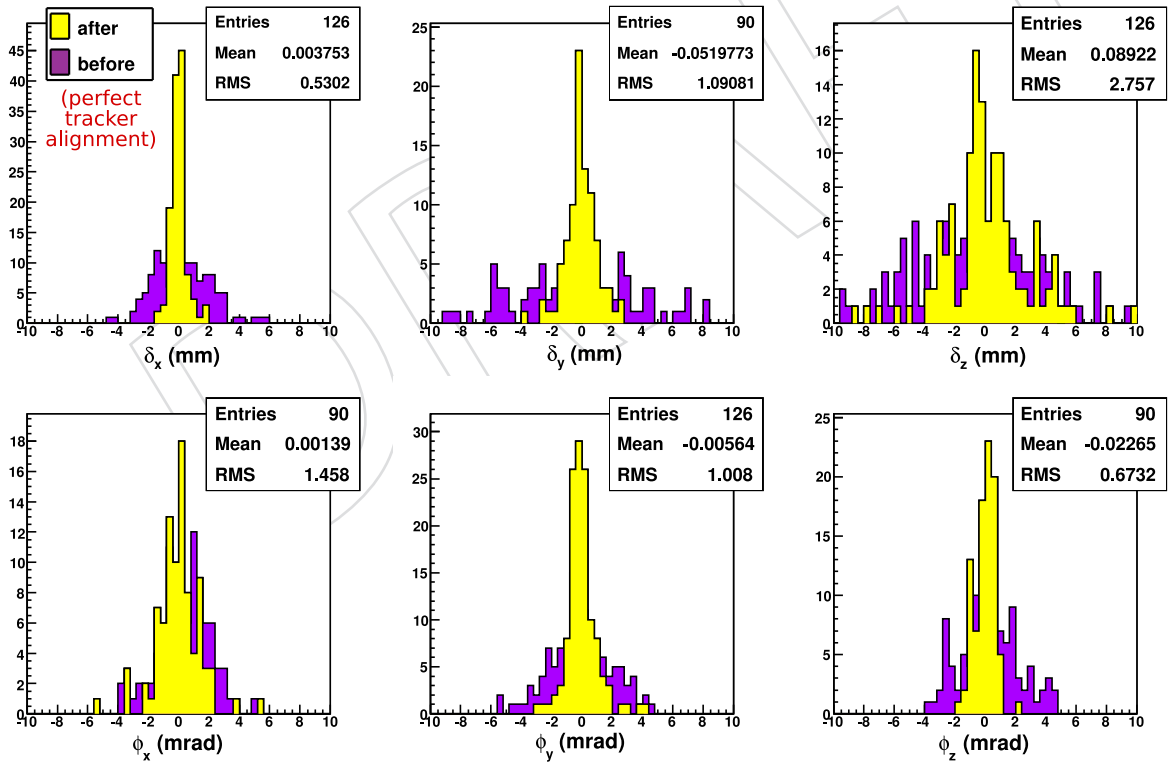
Further development of the MillePede algorithm is expected to reach a better accuracy by improving the error treatment in the covariance matrix E , and by improving the description of the tails of the residuals distributions.

4.4 Alignment Results and Cross-Checks

Both the HIP and MillePede algorithms were applied to align barrel wheels -1 , 0 , and $+1$, with the exception of sectors 1 and 7 (extreme horizontal sides of the detector) using the barrel section of the silicon tracker as the reference. The alignment was restricted to these chambers because they were the only ones sufficiently illuminated by the primarily vertical distribution of cosmic rays. We also restricted the input to high-quality $100 < p_T < 200$ GeV tracks with at least 15 tracker hits and a tracker reduced $\chi^2 < 10$. Loosening these cuts does not make



(a) HIP aligned-minus-true positions before (purple) and after (yellow) alignment.



(b) MillePede aligned-minus-true positions before (purple) and after (yellow) alignment.

Figure 9: Alignment with simulated cosmic rays using (a) HIP and (b) MillePede. Each entry in the histograms is the difference between the aligned and true values of alignment parameters for one chamber.

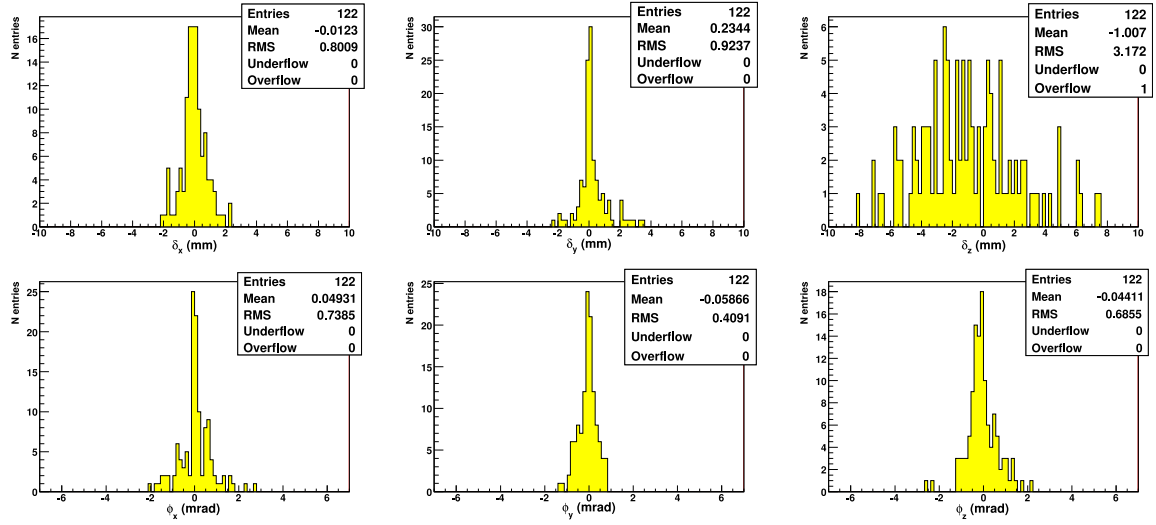


Figure 10: Differences in global alignment parameters between HIP and MillePede.

significantly more chambers available for alignment. With such high-momentum tracks, controlling for charge-antisymmetric effects such as magnetic field or material map errors makes negligible difference in the results ($100 \mu\text{m}$, 0.1 mrad). The dataset included all runs marked as acceptable for physics in the CMS run registry, with a magnetic field of 3.8 T.

In addition to the chambers explicitly excluded from alignment due to poor statistics, two chambers next to sectors 1 and 7 (in wheel, station, sector $(-1, 2, 8)$ and $(+1, 3, 8)$) had no tracks passing the cuts and two more ($(-1, 1, 12)$ and $(+1, 2, 2)$) failed to converge in HIP. These issues will not exist in alignments with ϕ -symmetric collisions data.

We checked our alignment results in four ways: we verified (1) that the algorithms optimized their intended expressions, (2) that they agree with one another, within the errors implied by the Monte Carlo study, (3) that the new global chamber positions yield better agreement with local measurements, and (4) that the new alignment yields better momentum resolution for tracks.

The simplest way to test (1) is to run the alignment algorithm a second time on the same dataset and verify that the second alignment corrections are always zero. As a sanity check, we also verified that the raw residuals distributions are centered on zero with very high precision. An example of this was shown in Figure 8.

Figure 10 compares the results from the two algorithms for each chamber, thereby demonstrating (2). Though the corrections relative to design geometry were on the order of 5–10 mm (due to effects such as gravitational sag), the two algorithms agree within expectations from Monte Carlo studies (Figure 9), and a factor of 2 better than expected in $\delta\phi_x$ and $\delta\phi_y$.

Local alignment measurements to test (3) were derived by extrapolating linear track segments from one chamber to another (in the same sector, neighboring stations). This verification procedure introduces information not used in the alignment itself, namely the higher precision with which tracks can be propagated over a short distance (1 meter) than a long distance (3–6 meters).

For this diagnostic, tracks were selected with $p_T > 50 \text{ GeV}$ and a correction was applied to cancel the effect of the magnetic field by taking advantage of the fact that positively- and

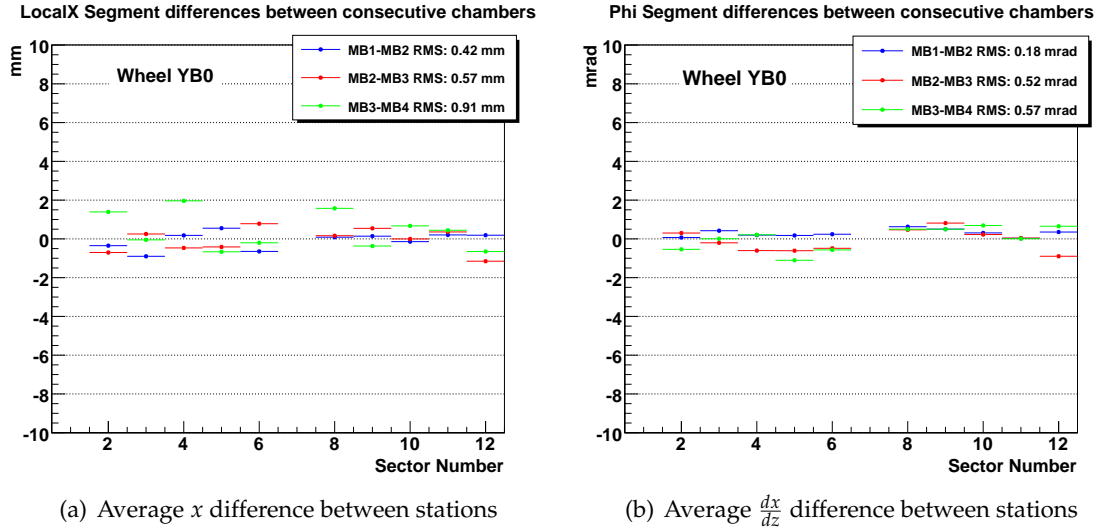


Figure 11: Validation of alignment by comparing track segments in neighboring chambers.

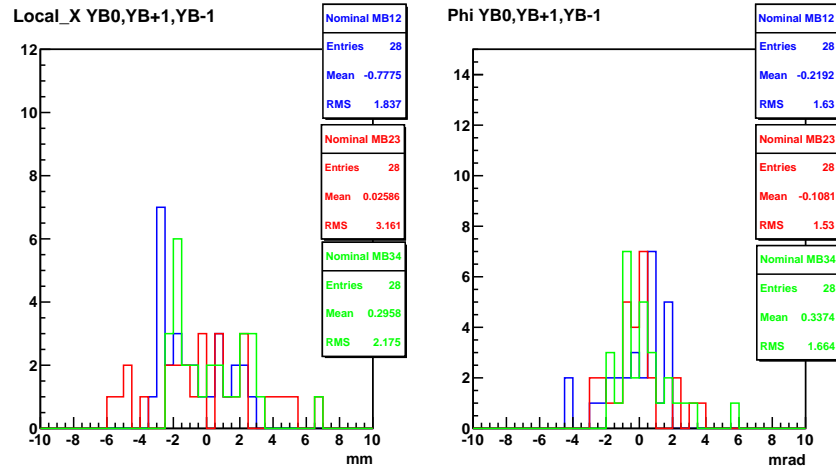
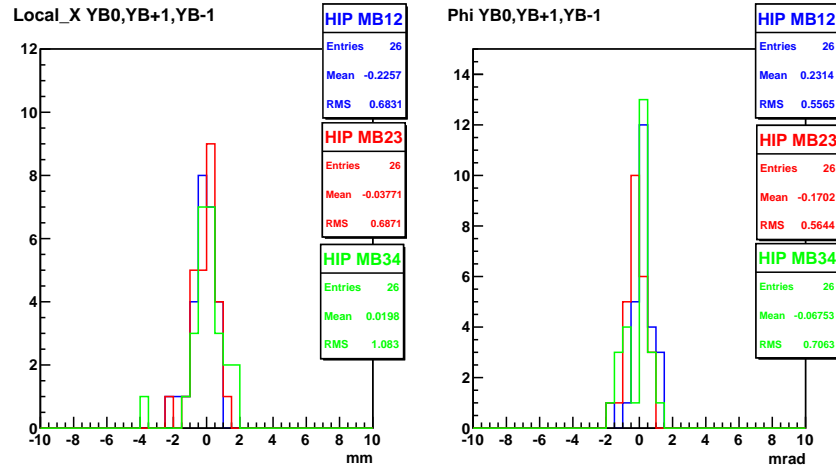
negatively-charged tracks are pushed in opposite directions. Figure 11 shows the level of agreement in x position and $\frac{dx}{dz}$ angle between segments in neighboring stations for each sector in wheel 0. To compare the initial state with the results of each algorithm in all wheels, we collected all of the comparisons into histograms, shown in Figure 12.

To verify that the new alignment (in this case, HIP only) improves momentum resolution, we selected cosmic rays with $p_T > 200$ GeV, split each into two tracks near the origin (similar to what would be observed in LHC collisions), and compared the momentum of the top and bottom fits. Since the cosmic ray was a single particle, any mismatch between the halves is purely instrumental. Cosmic rays have a steeply falling distribution, so most of the selected tracks have p_T close to 200 GeV. The alignment was performed using tracks with $100 < p_T < 200$ GeV tracks, so this is an independent sample. Figure 13 compares tracker-only tracks and tracks reconstructed with muon hits (first muon station only), before and after the muon alignment.

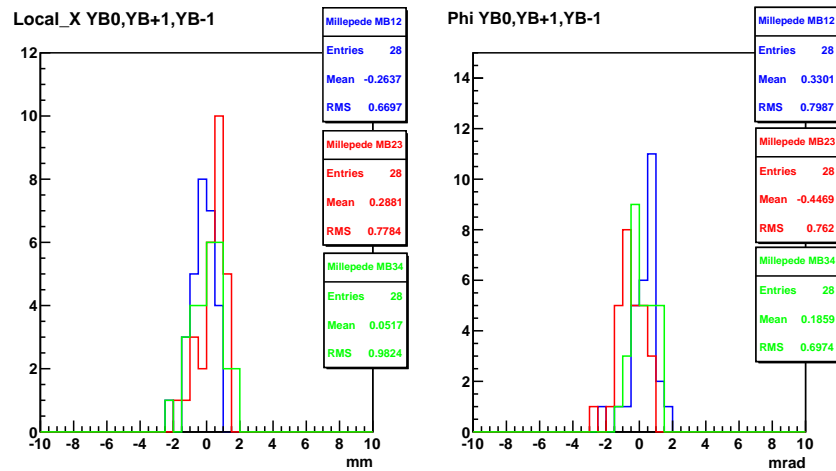
5 Conclusions

In this note, we have demonstrated a variety of procedures for aligning different parts of the muon system: layers in DT chambers, CSC chambers in rings, and global positions of DT chambers relative to the central tracker. We have fully exploited the available data, horizontal LHC beam-halo muons and vertical cosmic rays.

These procedures will be used without major modifications to re-align the muon system with muons from LHC collisions, once such data are available. The ϕ -symmetric distribution and broad coverage in η of collisions muons will allow us to extend the global alignment to all muon chambers, and reach about $400 \mu\text{m}$ precision in $r\phi$ from 50 pb^{-1} of data, according to simulations. Moreover, the ability to compare results from collisions and non-collisions samples, using global and local methods with the same dataset, will provide additional cross-checks. By verifying the muon alignment in as many ways as possible, we can add confidence to the muon momentum resolution at all energy scales, improving sensitivity to signatures of new physics.

(a) Before alignment **FIXME:** or design? "Before alignment" means CRAFT_V4

(b) Results from the HIP algorithm



(c) Results from the MillePede algorithm

Figure 12: Histograms of track segment comparisons: the number of entries is the number of sectors tested in the 3 wheels of this exercise.

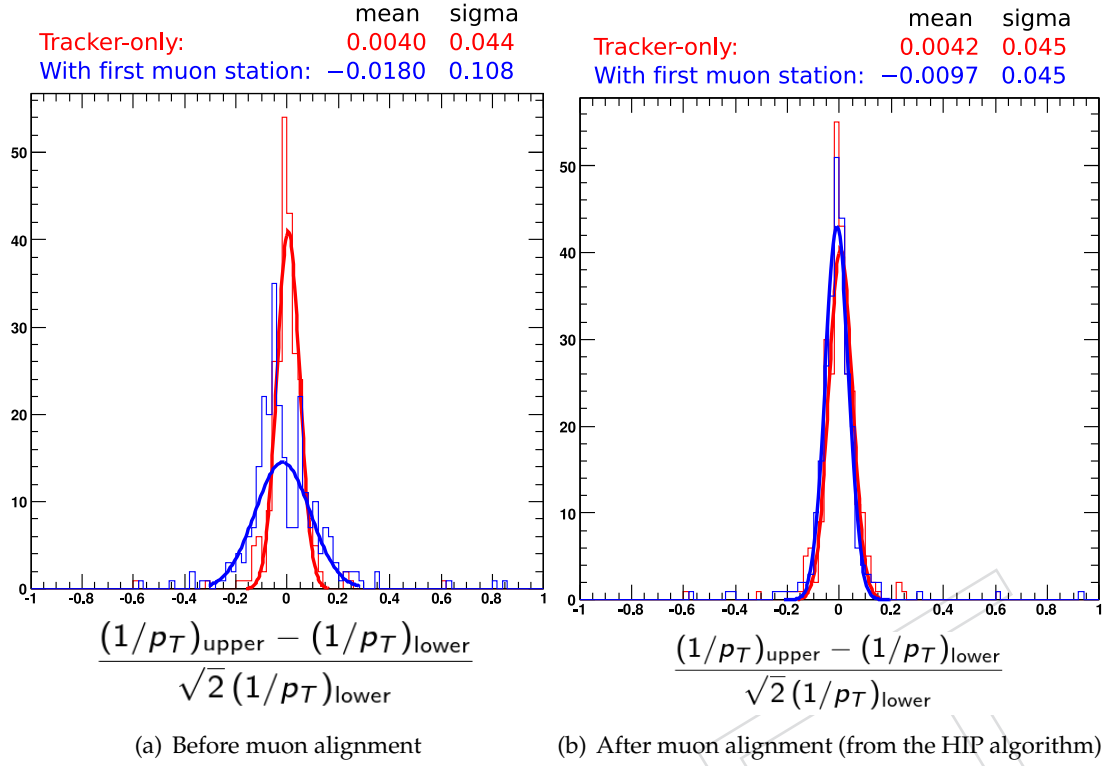


Figure 13: Top vs. bottom $1/p_T$ comparison for $p_T \gtrsim 200$ GeV split cosmic rays.

References

- [1] CMS Collaboration, "CFT-09-017," *J. Inst.* (2009).
- [2] "<https://twiki.cern.ch/twiki/bin/view/CMS/CMSConventions>,".
- [3] CMS Collaboration, "CFT-09-003," *J. Inst.* (2009).
- [4]
- [5] CMS Collaboration, "CFT-09-017," *J. Inst.* (2009).
- [6] CMS Collaboration, "CFT-09-017," *J. Inst.* (2009).